




# Silicon surface lattice resonances and halide perovskite semiconductors for exciton-polaritons at room temperature

DINH HAI NGUYEN,<sup>1,6</sup> SY KHIEM NGUYEN,<sup>1,6</sup> MINH QUAN TRAN,<sup>1</sup> VIET HOANG LE,<sup>1</sup> QUOC TRUNG TRINH,<sup>1</sup> SON TUNG BUI,<sup>2</sup> XUAN KHUYEN BUI,<sup>2</sup> DINH LAM VU,<sup>3</sup> HAI-SON NGUYEN,<sup>4,5</sup> AND QUYNH LE-VAN<sup>1,\*</sup> 

<sup>1</sup>College of Engineering and Computer Science, VinUniversity, Gia Lam district, Hanoi 14000, Vietnam

<sup>2</sup>Institute of Materials Science, Vietnam Academy of Science and Technology, 18 Hoang Quoc Viet, Hanoi, Vietnam

<sup>3</sup>Graduate University of Science and Technology, Vietnam Academy of Science and Technology, 18 Hoang Quoc Viet, Hanoi, Vietnam

<sup>4</sup>Univ Lyon, Ecole Centrale de Lyon, CNRS, INSA Lyon, Université Claude Bernard Lyon 1, CPE Lyon, INL, UMR5270, 69130 Ecully, France

<sup>5</sup>Institut Universitaire de France (IUF), Paris, France

<sup>6</sup>Contributed equally

\*quynh.lv@vinuni.edu.vn

**Abstract:** Owing to their high oscillator strength, binding energy, and low-cost fabrication, two-dimensional halide perovskites have recently gained attention as excellent materials for generating exciton-polaritons at room temperature. Unlike traditional materials used for polaritons, such as ZnO, GaAs, and GaN, halide perovskites exhibit great compatibility with matured CMOS technologies. However, no studies have reported perovskite-based polaritons on silicon platforms. Here, we numerically demonstrate the possibility of a polariton when a Si nanodisk array couples with a thin film of phenethylammonium lead iodide perovskite. An asymmetric lattice of thin Si nanodisks is used to generate surface lattice resonances from the coupling between the disk's electrical resonator and the lattice's diffracted waves. Polaritonic modes with high Rabi splitting values can be easily achieved for a large range of parameters. This Rabi splitting can be engineered by varying the ratio of electromagnetic energy confined within the Si disk and perovskite thin film. This study provides insight into nanophotonic structure design for CMOS-based optoelectronics, sensors, and polaritonic devices.

© 2022 Optica Publishing Group under the terms of the [Optica Open Access Publishing Agreement](#)

## 1. Introduction

Light-matter interactions have been investigated by generations of researchers owing to their uniqueness in fundamental physics and great potential in practical applications [1–3]. The essence of light-matter interactions is the coupling strength,  $g$ , which is used to classify weak or strong interactions. In the weak coupling regime,  $g < |\gamma - \kappa|/4$ , where  $\gamma$  and  $\kappa$  are the damping rates of the uncoupled optical modes and excitons, respectively [4,5]. During this process, no new state is created; however, the optical properties of quantum emitters are modified in terms of enhanced or inhibited radiations. Contrastingly, the strong coupling between light and matter ( $g > |\gamma - \kappa|/4$ ) is considered a reversible process in which the exchange rate between the cavity's photon density and the excitons of quantum emitters occurs periodically. The reversible process creates a new mixed state that is half-photon and half-exciton, called exciton-polaritons. The intriguing property of the polaritons is the possibility of collective relaxation to the ground state to form Bose-Einstein condensation, which is accompanied by coherent radiation that does not require an inverse photon

population. Thus, it enables low-threshold lasers. The realization of room-temperature polaritons is a real challenge due to the stringent requirements of excitons with large oscillator strength for enhanced couplings and high binding energy for room-temperature polaritons. Hence, room temperature polaritons have been realized only in a few classes of materials, including ZnO [6–8], transition metal dichalcogenides [9–15], and organic semiconductors [16,17]. The inorganic semiconductors possess a strong Coulomb potential and offer Wannier-Mott excitons in which electrons and holes are weakly bound across several lattice sites, thereby preventing the relaxation mechanisms of polariton at large population densities [18,19]. On the other hand, excitons in organic semiconductors are tightly confined Frenkel excitons within the volume of a single molecule, thereby allowing large binding energy and strong oscillator strength of the excitons [20]. Metal halide-based perovskites, a unique class of semiconductors containing group VII elements, such as Br and I, provide remarkably combined properties from organic and inorganic semiconductors for a strong coupling study [21,22]. Similar to inorganic excitons, perovskite excitons are of the Wannier-Mott type, thus exhibiting giant nonlinearity features compared to the Frenkel excitons in organic materials. However, similar to organic excitons, perovskite excitons possess very high binding energy of a few hundred meV and strong oscillator strength for light-matter interactions. These unique features of perovskites are ideal to study exciton-polariton at room temperature. To date, perovskites-based polaritons have been proposed and realized only in traditional microcavities [23–25], surface plasmon polaritons [26,27], micro/nanowires [28,29], and all-perovskite lattices [30–32]. Nonetheless, unlike the traditional excitonic materials for strong couplings, such as ZnO, GaAs, or GaN, a high-quality perovskite layer can be achieved via an all-solution-based process, thus enhancing this material's compatibility with matured CMOS technology having low-cost fabrication requirements. Harnessing polaritons at room temperature by spin-coating a thin film perovskite layer onto a processed silicon layer of a CMOS chip would be ideal to build future polaritonic devices. Recent studies have reported the surface lattice resonances (SLRs) of structured Si to achieve polaritons using organic molecules [33,34] and those of Ag structures using perovskites for conventional lasing [35]. However, owing to high refractive indexes of perovskites, perovskite-based polaritons on the patterned silicon platform or even broader SLR-supported system are yet to be investigated.

In this study, a Si nanodisk array has been numerically analyzed to realize strong coupling with a two-dimensional halide perovskite. The metasurface is composed of a two-dimensional array of Si nanodisks on a sapphire substrate. A thin film of phenethylammonium lead iodide (PEPI) perovskite ( $C_6H_5C_2H_4NH_3)_2PbI_4$ ) covers the metasurface. The resonant Si particles are shown to radiatively couple with the diffraction orders of lattice using Rayleigh anomalies to form SLRs whose origin is investigated using multipole decomposition analysis. The polaritons are shown to be easily achievable using positive and negative detuning of the coupling. The results indicate that the Rabi splitting values can be manifested by engineering the ratio of the electric fields confined within the Si structures and perovskite layer. Finally, we discuss the minor role of the Q-factor of photonic modes in determining the Rabi splitting values.

## 2. Design and photonic modes in passive materials

A two-dimensional lattice of Si nanodisks is designed on a sapphire substrate ( $n = 1.76$ ) to focus on the SLRs while eliminating the waveguide-induced modes [36]. The schematic of the sample is shown in Fig. 1(a). Si nanodisks with the height  $h = 30$  nm and radius  $r = 56$  nm are selected, and their periodicities in the  $x$ - and  $y$ -directions are  $p_x = 260$  nm and  $p_y = 320$  nm, respectively. We use a thin layer of PEPI perovskite that forms multiple quantum wells owing to the intertwined bandgaps of the organic and inorganic compounds, as shown in Fig. 1(a). The excitons are formed in the inorganic layers and confined by the surrounding organic layers because of a reduction in lateral space and dielectric confinement. The combined confinements produce a high binding energy of the perovskites' excitons, which is up to 200 meV at room temperature [37,38].

Additionally, the perovskite exhibits a well-defined peak in the absorption spectrum, which is a signature of its large oscillator strength [39]. The excitonic properties of the perovskite can be also inferred using relative permittivity. The optical properties of the PEPI perovskites were imported by experimental values [40] and displayed in Fig. 1(b). A pronounced peak appearing in the imaginary part of the permittivity indicates a large binding energy of the exciton whose dielectric function can be described by the Lorentz model:  $\epsilon_p(\omega) = n_\infty^2 + A/(E_X^2 - E^2 + i\Gamma_X E)$ , where  $n_\infty = 2.4$  is the refractive index of passive material,  $E_X = 2.4\text{eV}$  is the excitonic energy, and  $\Gamma_X = 0.03\text{eV}$  is the homogeneous linewidth of PEPI perovskites with the oscillator strength  $A = 0.4\text{eV}^2$  [27]. In our work, a passive design refers to the same structure; however, the perovskite material is replaced by a dielectric material with only a real refractive index  $n_\infty$  (the excitonic resonance is taken out). The permittivity of Si is obtained from Ref. [41]. The system was modeled using a commercial finite element simulator (Comsol Multiphysics, WaveOptics Module). A plane wave was excited atop the structure with Floquet's boundary conditions, and the reflectivity occurring at the same port was probed. When the thickness of perovskites is tuned in the common range of perovskite-based optoelectronics (50 nm to 500 nm, see Fig.S1, Supplement 1), an optimal thickness to excite the SLRs is around 200 nm.

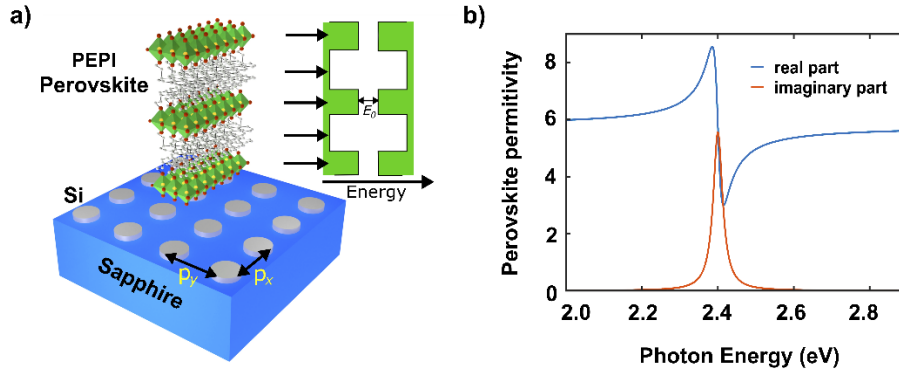


**Fig. 1.** a) Schematic diagram of a rectangular lattice of Si nanodisks on a sapphire substrate covered by a thin layer of PEPI perovskite. The periodicity in the short and long axes are  $p_x = 260\text{nm}$  and  $p_y = 320\text{nm}$ , respectively. The thin film (200 nm) of perovskite has an intertwined architecture of organic and inorganic layers forming quantum wells.  $E_0$  denotes the bandgap energy between the conduction and valance bands. b) Dielectric functions of PEPI perovskite indicate a pronounced exciton at 2.4 eV.

The properties of SLR modes in the passive design are discussed as follows. A plane wave is excited atop the structure with Floquet's boundary conditions and the reflectivity at the same port is probed. Because the lattice is rectangular, the dispersion relation would be different based on the projected axis of the incident waves. Consider the incident angle,  $\theta$ , with respect to the normal axis; thus, the dispersion of SLRs corresponding to the incident planes xOz and yOz obeys the following equations 1(a) and 1(b), respectively:

$$k_s^2 = p^2 \left( \frac{2\pi}{p_x} \right)^2 + q^2 \left( \frac{2\pi}{p_y} \right)^2 + p \frac{4\pi}{p_x} k_x + k_x^2 \quad (1a)$$

$$k_s^2 = p^2 \left( \frac{2\pi}{p_x} \right)^2 + q^2 \left( \frac{2\pi}{p_y} \right)^2 + q \frac{4\pi}{p_y} k_y + k_y^2 \quad (1b)$$

where  $k_s$  and  $k_{x,y} = \frac{2\pi}{\lambda} \sin\theta$  are the scattered and incident wave numbers in x- and y- directions, and  $(p,q)$  are integers defining the in-plane diffraction orders, (also known as Rayleigh anomalies

(RAs)). The SLR is a hybrid mode between the resonators and diffracted waves; hence, it is evident in the RA of scattering spectra. Particularly, we focus on the lowest energy modes corresponding to the first diffraction orders, i.e.,  $|p + q| = 1$ . These modes consist of four couples  $(0,1)$ ,  $(0,-1)$ ,  $(1,0)$ , and  $(-1,0)$  of  $(p,q)$  corresponding to the two pairs of SLR modes  $\text{SLR}(\pm 1,0)$  and  $\text{SLR}(0,\pm 1)$  that are perpendicularly polarized requiring the  $y$ - and  $x$ -polarized excitation light, respectively, for any incident plane. At normal incidence (i.e.  $k_{x,y} = 0$ ), Eq. (1)(a,b) indicates that the offset energies of  $\text{SLR}(\pm 1,0)$  and  $\text{SLR}(0,\pm 1)$  are imposed by the periods  $p_x$  along  $x$ -direction and  $p_y$  along  $y$ -direction, respectively (see Supplement 1 for more details). Therefore, the detuning of  $\text{SLR}(\pm 1,0)$  and  $\text{SLR}(0,\pm 1)$  can be determined independently with respect to the excitonic resonance using  $p_x$  and  $p_y$ , respectively, i.e., the splitting between  $\text{SLR}(\pm 1,0)$  and  $\text{SLR}(0,\pm 1)$  can be controlled via the anisotropy ratio  $p_x/p_y$ . Figure 2(a) shows the variation in offset energies of the two pairs while scanning the anisotropy ratio. Here, the  $\text{SLR}(\pm 1,0)$  and  $\text{SLR}(0,\pm 1)$  at  $k = 0 \mu\text{m}^{-1}$  are excited by an electric field polarized in  $x$ - and  $y$ -directions, or Pol- $x$  and Pol- $y$ , respectively. The individual reflectivities are then combined and normalized to form Fig. 2(a). The ratio  $p_x/p_y$  is scanned by simultaneously tuning the  $p_x$  and  $p_y$  while fixing their sum which is equal to  $580 \text{ nm}$ . Evidently,  $\text{SLR}(\pm 1,0)$  and  $\text{SLR}(0,\pm 1)$  intersect at  $p_x/p_y = 1$  and split when a small anisotropy is introduced. At oblique incidence,  $\text{SLR}(\pm 1,0)$  remains degenerated along  $k_y$  with parabolic dispersion (see Eq. (1b)), whereas the degeneracy of  $\text{SLR}(\pm 1,0)$  is lifted along  $k_x$ , thereby exhibiting linear energy-momentum dispersions of opposite group velocities (see Eq. (1a)). Similarly,  $\text{SLR}(0,\pm 1)$  remains degenerated along  $k_x$  with parabolic dispersion (see Eq. (1a)) while splits into linear dispersions of opposite group velocities along  $k_y$  (see Eq. (1b)). For both pairs, the parabolic/linear dispersion along  $k_x$  transforms to linear/parabolic dispersion along  $k_y$  [42].

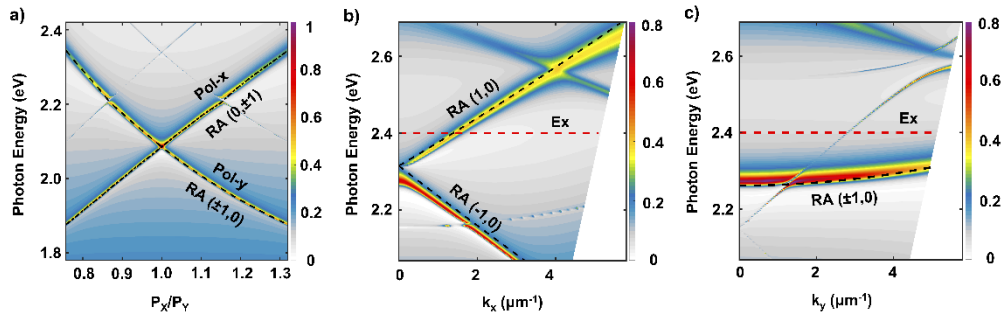


**Fig. 2.** a) The surface lattice resonances of the Si nanodisk arrays as a function of the asymmetric ratio. They are excited at  $k = 0 \mu\text{m}^{-1}$  using electric fields in  $x$ - (Pol- $x$ ) and  $y$ - (Pol- $y$ ) directions. b) The resonator couples with in-plane diffraction orders  $(\pm 1, 0)$  in  $x$ -direction. c) SLR of the arrays when the resonator couples with diffraction  $(0, \pm 1)$  in  $y$ -direction. The red dashed lines in b) and c) indicate the position of the exciton (Ex) of perovskites.

Because  $\text{SLR}(\pm 1,0)$  and  $\text{SLR}(0,\pm 1)$  behave similarly and their detuning with respect to the excitonic resonance can be independently addressed, the rest of the paper focuses on  $\text{SLR}(\pm 1,0)$  without losing the generality. To numerically investigate these modes, the angle-resolved reflectances of the passive metasurface with  $p_x = 260 \text{ nm}$  and  $p_y = 320 \text{ nm}$  are shown in Figs. 2(b) and 2(c), respectively, which are excited using  $y$ -polarized light along  $k_x$  and  $k_y$ . The energy of PEPI exciton (i.e.  $E_X = 2.4 \text{ eV}$ ) is indicated by dashed red lines in Figs. 2(b,c). The analytical calculations of Rayleigh anomalies for corresponding diffraction orders are denoted by dashed black lines. Figure 2(c) indicates that the parabolic dispersion along  $k_y$  of  $\text{SLR}(\pm 1,0)$  is almost dispersionless; hence, it is not suitable for studying the strong coupling regime. Contrarily, the

linear dispersion along  $k_x$  of SLR( $\pm 1,0$ ) is of high group velocities [Fig. 2(b)]. Particularly, SLR (1,0) intersects the excitonic resonance at  $k_x = 1.38\mu\text{m}^{-1}$ , thus being a good candidate for investigating the anti-crossing feature of the strong coupling regime in active structures. Figure 3(a) shows the photonic mode designed to achieve exciton polariton using PEPI perovskites. The two modes SLR( $\pm 1,0$ ) are monitored for different incident angles, as indicated by the two dispersive peaks (black dashed lines). The SLR(1,0) crosses the exciton at  $7^\circ$ , denoted by the point  $A_2$  in the spectrum. The peak  $A_1$  marks the SLR(-1,0) of the lattice at the same angle. The corresponding electric field intensities are presented in Fig. 3(b). These field distributions reveal the formation of the diffracted waves extending to the edges of the unit cell when the resonances of the Si nanodisk couple with the in-plane diffracted orders of the lattice.

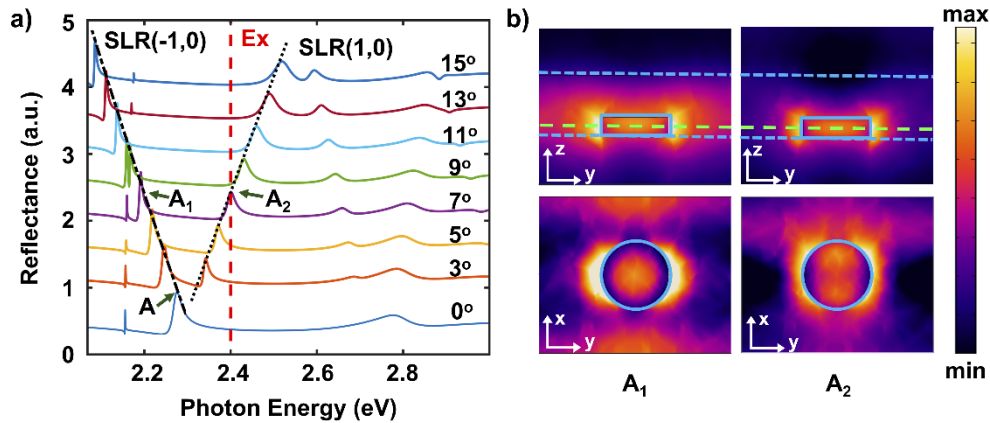


**Fig. 3.** a) Simulated reflectance spectra of the Si metasurface probed in  $x$ -direction under varied oblique incident angles.  $A$  is the SLR of  $p_x$  when the resonator of the Si nanodisk couples with grazing diffracted waves.  $A_1$  and  $A_2$  are degeneracy of point  $A$  as the incident angle increases. b) The electric fields of SLRs (points  $A_1$  and  $A_2$ ) when they are excited at  $7^\circ$  with respect to the normal axis. The upper panels show normalized E-fields at the side view truncated at the middle of the Si nanodisk, whereas the lower ones show the normalized E-fields at the middle plane of the disk (green dash lines). The cyan dash lines indicate the interfaces between layers.

To gain insight into the formation of SLR( $\pm 1,0$ ), the multipole decomposition of the Si nanodisk array embedded in the passive layer is calculated. It is known that a miniaturized high-index structure can support both electrical and magnetic resonances as a result of efficient coupling of the displacement current inside the resonator and external electromagnetic waves. The nature of resonances can be described using the Mie theory [43–45]. Previous studies of dielectric resonators indicated that the electrical and magnetic resonances associated with Si nanostructures could be tuned independently by altering the geometric parameters and optical environmental settings [46–52]. The scattering coefficient of the proposed structure [ Fig. 4(a)] is calculated using the multipole analysis from an electric charge-current distribution, as proposed in Ref. [53]. Here, the periodic boundary condition and diffraction orders are implemented to consider the lattice effect. Among the first and second order electric and magnetic resonances, the proposed structures are governed by the electric resonance because of the small Si thickness. Peak C (2.787 eV) is attributed to the cylinder's electric dipole response. The radiative coupling of the electric dipole with the first diffracted wave (peak B at 2.157 eV) produces the SLR (peak A at 2.279 eV). To verify the accuracy of the multipole decompositions, the SLR excitation at  $0^\circ$  is shown in Fig. 4(b). A good agreement of the spectral positions of peaks (A, B, and C) is obtained in the reflectance spectrum, which indicates a strong correlation between the multipole

contribution calculation and simulated reflectance spectrum. The multipole decomposition indicates the three emerging resonance peaks contributed by electric dipole radiation of the Si nanodisk coupled with the first diffraction orders of lattices.

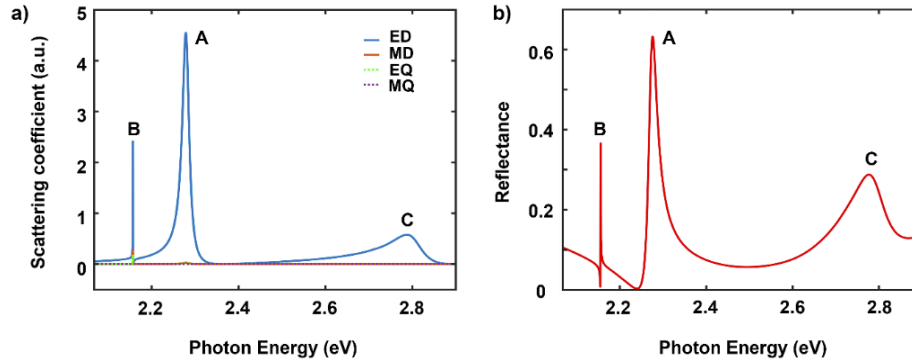


**Fig. 4.** a) Contribution of each multipole to the scattering efficient of the Si lattice. The calculation is based on expressions for the multipolar decomposition of an electric charge–current distribution from Ref. [33], which incorporates the lattice effect. The geometric parameters of Si nanodisk are: radius  $r = 56$  nm, height  $h = 30$  nm, while the lattices in  $x$ - and  $y$ -axes are 260 nm and 320 nm, respectively. b) Reflectance spectrum of the Si metasurface at normal incidence.

### 3. Polaritonic modes in active materials

Herein, we investigate the strong coupling regime between the aforementioned SLRs and PEPI excitonic resonance in the active structure (i.e., the imaginary part of the permittivity of the PEPI layer is taken into account). Figure 5 shows the angle-resolved reflectivity spectra along  $k_x$  under  $y$ -polarized excitations. We make the following observations:

- A dispersionless resonance signal at 2.4 eV indicates the fraction of PEPI excitons that do not couple with the photonic modes.
- The strong coupling regime is indicated by an avoided crossing observed at  $k_x = 1.38 \mu\text{m}^{-1}$  between the two modes  $\text{LP}_1$  and  $\text{UP}_1$  for the lower and upper polariton branches, respectively. These polaritonic modes originate from the hybridization of  $\text{SLR}(1,0)$  and PEPI excitons. A Rabi splitting of  $\Omega_1 = 230 \text{ meV}$  is extracted from the splitting of these two modes at the avoided crossing momentum.
- Another pair of polariton branches, i.e.,  $\text{LP}_2$  and  $\text{UP}_2$  (with resonance signal less pronounced), is originated from the strong coupling between  $\text{SLR}(-1,0)$  and PEPI excitons. Because the  $\text{SLR}(-1,0)$  does not cross the excitonic energy in passive structure [see Fig. 2(b)], there is no avoided crossing point for  $\text{LP}_2$  and  $\text{UP}_2$ . Therefore, the Rabi splitting energy is not “visible” in these spectra. However, the bending of the  $\text{UP}_2$  band near the exciton energy at high wavevectors is a hallmark of the strong coupling regime, and clearly indicates the conversion from photonic-like at low wavevectors to excitonic-like at high wavevectors of this mixed state.

We now implement a simple effective theory to explain the observed coupling mechanisms, noting that all polaritonic modes can be calculated rigorously using a fully quantum model-mechanical formalism [54,55]. Because excitons are uniformly and randomly distributed in the PEPI film, the nature of their coupling with the SLRs can be different depending on their location

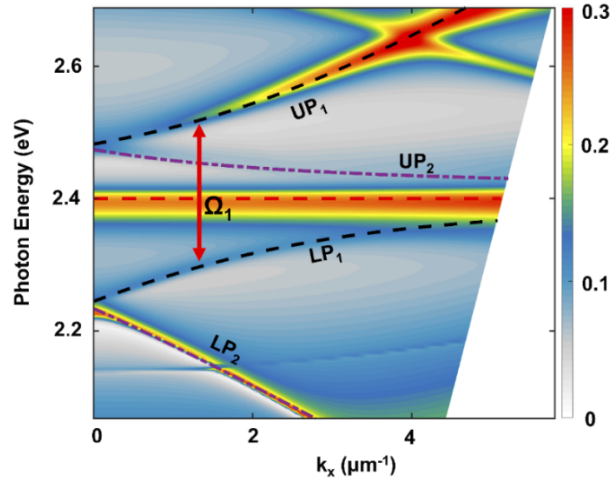


**Fig. 5.** Angle-resolved reflectance of the Si nanodisk array coupled with perovskites. Two avoided crossing points are observed at  $k = 1.38 \mu\text{m}^{-1}$ . The first Rabi splitting  $\Omega_1$  results from a negative detuning between the SLR(1,0) and excitons of the perovskites, thereby forming the upper branch of polariton (UP<sub>1</sub>) and lower branch of polariton (LP<sub>1</sub>). From this reflectivity, the extracted value of  $\Omega_1$  is 230 meV. Other polaritons are created owing to the interaction between SLR (-1,0) and the exciton. The avoided crossing is not observed owing to the absence of crossing between them.

with respect to the SLR( $\pm 1,0$ ) hot spots [i.e. positions of strong intensities in Fig. 3(b)]. A significant fraction of excitons resides outside the field hot spots and cannot be efficiently coupled with the SLRs. They are responsible for the dispersionless resonance in Fig. 5. The excitons in the vicinity of field hot spots can undergo the strong coupling regime with SLRs. However, these excitons cannot strongly couple with both SLR modes because the hot spot locations of SLR(1,0) overlap with cold spot locations of SLR(-1,0) and vice-versa. Consequently, these excitons can be divided into the following two types: one half coupling strongly with the SLR (1,0) and another half with SLR (-1,0). Thus, the polaritonic modes are described by an eigen-problem of four coupled oscillators, given as follows [27]:

$$\begin{bmatrix} E_X - i\Gamma_X & g_{10} & 0 & 0 \\ g_{10} & E_{10} - i\Gamma_{10} & 0 & 0 \\ 0 & 0 & E_X - i\Gamma_X & g_{-10} \\ 0 & 0 & g_{-10} & E_{-10} - i\Gamma_{-10} \end{bmatrix} \begin{bmatrix} \alpha_{10} \\ \beta_{10} \\ \alpha_{-10} \\ \beta_{-10} \end{bmatrix} = E \begin{bmatrix} \alpha_{10} \\ \beta_{10} \\ \alpha_{-10} \\ \beta_{-10} \end{bmatrix} \quad (2)$$

where  $E_X$ ,  $E_{10}$ , and  $E_{-10}$  are the energies of the exciton, SLR(1,0), and SLR(-1,0), respectively.  $\Gamma_X$ ,  $\Gamma_{10}$ , and  $\Gamma_{-10}$  represent the dissipate rates of the exciton and collective resonances.  $E$  is the eigenvalue energy of the polaritonic modes.  $\alpha_{\pm 10}$  and  $\beta_{\pm 10}$  are the respective Hopfield coefficients of the excitons and photonic modes that constitute the polaritons. The fitting of UP<sub>1</sub> and LP<sub>1</sub> polaritonic modes (black dashed lines in Fig. 5) corresponds to a Rabi splitting of  $\Omega_1 \approx 2g_{10} = 222\text{meV}$  that commensurates with the extracted values from the numerical simulations of reflectivity spectra and it is in good agreement with the typical Rabi splitting of PEPI-based polaritons [30]. Furthermore, the fitting of UP<sub>2</sub> and LP<sub>2</sub> branches (purple dashed lines) allow us to obtain the second Rabi splitting  $\Omega_2$  that cannot be directly extracted from

numerical simulations. The obtained value of  $\Omega_2$  is 6 meV smaller than that of  $\Omega_1$ , thereby indicating that the coupling strengths  $g_{10}$  and  $g_{-10}$  are practically equal. The similar coupling strengths are in accordance with the fact that (1,0) and (-1,0) are first diffraction orders coupled with the same electric dipole mode.

The mixed exciton-photon nature of the polaritonic states is quantified by the excitonic fractions  $|\alpha_{\pm 10}|^2$  and photonic fractions  $|\beta_{\pm 10}|^2$  that are calculated using the Hopfield coefficients obtained from the fittings of the four polaritonic modes. Furthermore, the excitonic and photonic fractions are plotted in Fig. 6 as functions of the wavevector  $k_x$ . Crossing points of excitonic and photonic fraction curves at  $k_x = 1.38 \mu\text{m}^{-1}$  in Figs. 6(a,b) indicate a balance of 50%-50% of exciton-photon hybridization for  $\text{LP}_1$  and  $\text{UP}_1$  at the avoided crossing point. The crossing points between fraction curves are not observed in Figs. 6(c,d) owing to the absence of avoided crossing point between  $\text{LP}_2$  and  $\text{UP}_2$ . However, these states exhibit mixed exciton-photon behaviour with the highest hybridization of 28%-72% at  $k_x = 0$ .

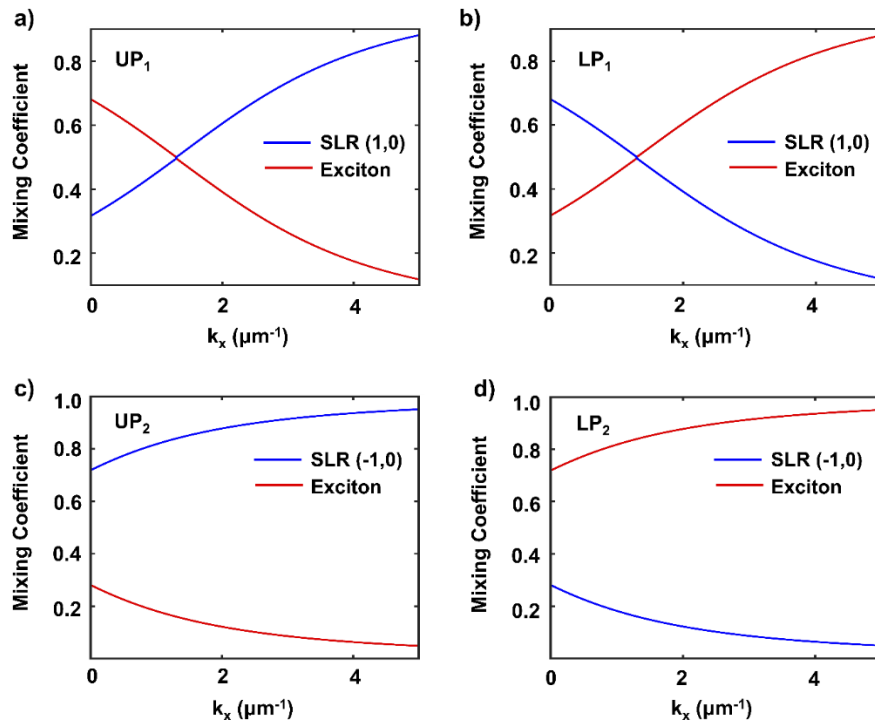


**Fig. 6.** a) Hopfield coefficients for polaritons in Si nanodisk array with PEPI perovskites. The linear composition of excitons or SLR modes in each polariton branch are shown. a) and b) indicate the compositions of upper and lower polariton bands created by the coupling between SLR(1,0) and the excitons. c) and d) indicate the compositions of the upper and lower polaritons from a positive detuning.

The strong coupling mechanism is engineered by tuning the geometry of the Si nanodisks in which the photonic losses of the passive structure and avoided crossing point between  $\text{LP}_1$  and  $\text{UP}_1$  of the active structure are monitored for different nanodisk sizes. The disk thickness (30 nm) is kept constant to conserve the original physics of the Si lattice. The nanodisk radius is scanned from  $r = 30$  nm (filling factor,  $ff = 1\%$ ) to  $r = 111$  nm ( $ff = 14\%$ ), where the filling factor  $ff$  is defined as the volume of the Si cylinder divided by the unit cell volume of the perovskite layer (320 nm x 260 nm x 200 nm). Figure 7(a) represents the Q-factor of the passive structure and Rabi splitting as a function of the filling factor. The results indicate that the passive quality



factor decreases with increasing  $ff$ , which can be nicely fitted using the following quadratic law:  $Q(ff) = Q_0 + \frac{\alpha}{ff^2}$  where  $Q_0 = 37$  and  $\alpha = 0.1$ . This simple dependence of the quality factor can be explained as a quasi-bound state in the continuum behaviors. Indeed, for  $ff=0$ , the passive structure only consists of a lossless dielectric slab ( $n=2.4$ ) on sapphire. Thus, the photonic mode is a lossless guided mode with an infinite quality factor  $Q(ff=0) = \infty$ . This perfect photonic bound state is perturbed when the silicon disks are implemented (i.e. non-zero  $ff$ ) and it becomes leaky via radiative channels (i.e. radiation to the free space) and non-radiative channels (i.e. absorption of Si). Such perturbations produce a quasi bound state in the continuum situation that usually exhibits quadratic decline law as a function of the perturbation strength. For high values of filling factor, the structure can be assimilated as a lossy silicon slab on top of a lossless dielectric slab on sapphire, having  $Q_0$  as quality factor.

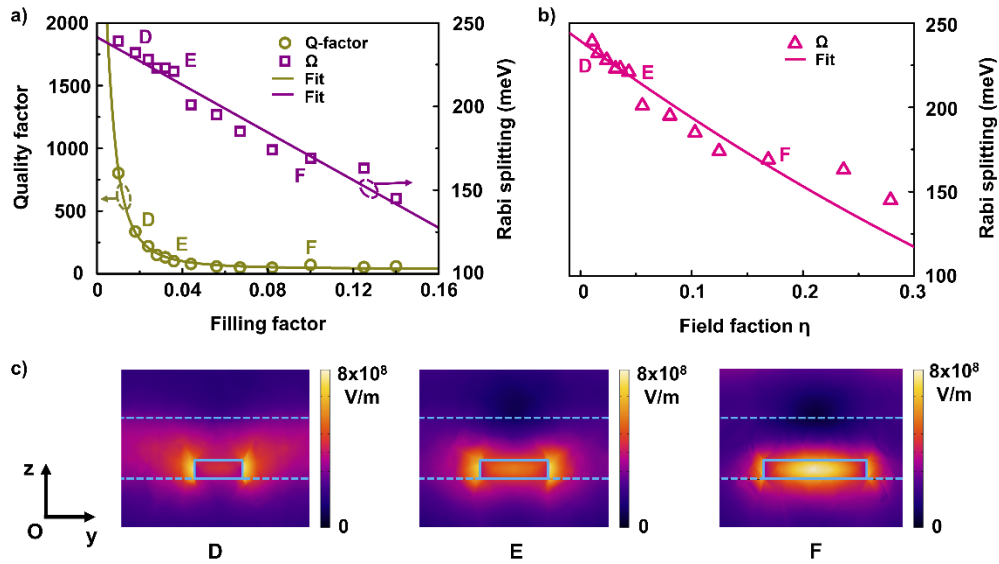


**Fig. 7.** a) Correlation between quality factor and Rabi splitting as a function of filling factor. b) Rabi splitting ( $\Omega_1$ ) of the polariton is shown as a function of the field fraction  $\eta$ . The field fraction is defined by a ratio of electric field confined in the Si disk to that of the PEPI thickness. c) The electric field distribution crosses the unit cell at points D, E, and F. A stronger energy confined in the Si disks leads to a decrease of the electromagnetic energy interacting with the exciton. It results in a decline of the Rabi splitting.

The Rabi splitting as a function of the filling factor is shown in Fig. 7(a), which decreases with increasing filling and it can be fitted using the following linear decreasing law:  $\Omega(ff) = \Omega_0(1 + \beta \cdot ff)$ , where  $\Omega_0 = 244$  meV and  $\beta = -2.9$ . Particularly,  $ff=0$  corresponds to the structure of a PEPI waveguide on sapphire and  $\Omega_0$  is the Rabi splitting of polaritonic modes arising from the strong coupling between photonic guided mode and PEPI excitons. The distinct features of the Rabi splitting and Q-factor in the same variation of the filling factor indicate that the quality of the photonic mode plays a trivial role in the determination of Rabi splitting strength, which is consistent with a recent study on the all-perovskite polariton [21,56]. The electric fields in the lattices are analyzed to gain insights into the contradictory features of Rabi splitting as the geometry of the cylinders is tuned. We calculate the field fraction,  $\eta$ , between electric fields confined within the Si cylinder ( $\mathcal{E}_{Si}$ ) and those confined in the perovskite slab  $\mathcal{E}_p$ ; hence, the normalized  $\eta = \frac{\int_{V_{Si}} |\mathcal{E}_{Si}| dV}{\int_{V_p} |\mathcal{E}_p| dV}$ . The Rabi splitting as a function of the field fraction is shown in Fig. 7(b). The numerical results are in agreement with the formula  $\Omega(\eta) = \Omega_0(1 - \eta)^2$  without

any more fitting parameters, where  $1 - \eta$  is the fraction of the electric field confined in the perovskite. If the energy ( $\propto \mathcal{E}^2$ ) is confined in the perovskite slab, the exciton-SLR couplings are enhanced. Consequently, the Rabi splitting is relatively stable, provided that the energy remains in the perovskite layer. As the disk diameters are increased, a shift in the energy confinement is observed inside the Si nanodisks, thereby resulting in a less interactive energy between the SLR and excitons and decreasing the Rabi splitting. The evolutions of energy confinement with increasing disk radius at several representative points (D, E, F) are shown in Fig. 7(c).

#### 4. Conclusions

In summary, we proposed a system of thin Si metasurfaces on a sapphire substrate to realize exciton polariton at room temperature for a thin film of halide perovskite. The optical properties of a Si crystalline are used to excite the resonances in a rectangular lattice of Si nanodisks, which emerge when the electric dipole radiation of the Si nanodisk is coupled with the grazing waves in lattices. The asymmetric lattice of Si nanodisks was designed to separate photonic modes and allow individual investigation of their roles in the formation of exciton polariton. The Rabi splitting (larger than 200 meV) was numerically demonstrated to be easily achievable for the perovskite thin film. Furthermore, engineering the confined energy in the perovskite thin film is crucial in controlling the Rabi splitting. The system can be fabricated using commercial Si on Sapphire (SOS) substrates and low-loss a-Si [57]. These findings are important designing strategies for implementing sensing and polaritonic devices. Other than the regular cylindrical lattices, more complex lattices can be engineered. Various concepts, such as bound states in the continuum (BIC) and quasi-BIC, can be used to engineer higher quality factor for sensing and polaritonic devices and photonic band dispersion.

**Funding.** Quy Doi moi sáng tạo Vingroup (VINIF.2021.DA00169).

**Disclosures.** The authors declare no conflicts of interest

**Data Availability.** Data underlying the results presented in this paper are not publicly available at this time but may be obtained from the authors upon reasonable request.

**Supplemental document.** See [Supplement 1](#) for supporting content.

#### References

1. P. Törmä and W. L. Barnes, "Strong coupling between surface plasmon polaritons and emitters: A review," *Rep. Prog. Phys.* **78**(1), 013901 (2015).
2. T. W. Ebbesen, "Hybrid light-matter states in a molecular and material science perspective," *Acc. Chem. Res.* **49**(11), 2403–2412 (2016).
3. D. D. Solnyshkov, G. Malpuech, P. St-Jean, S. Ravets, J. Bloch, and A. Amo, "Microcavity polaritons for topological photonics [Invited]," *Opt. Mater. Express* **11**(4), 1119–1142 (2021).
4. V. Savona, L. Andreani, P. Schwendimann, and A. Quattropani, "Quantum well excitons in semiconductor microcavities: Unified treatment of weak and strong coupling regimes," *Solid State Commun.* **93**(9), 733–739 (1995).
5. L. C. Andreani, G. Panzarini, and J.-M. Gérard, "Strong-coupling regime for quantum boxes in pillar microcavities: Theory," *Phys. Rev. B* **60**(19), 13276–13279 (1999).
6. M. Zamfirescu, A. Kavokin, B. Gil, G. Malpuech, and M. Kaliteevski, "ZnO as a material mostly adapted for the realization of room-temperature polariton lasers," *Phys. Rev. B* **65**(16), 161205 (2002).
7. H. Franke, C. Sturm, R. Schmidt-Grund, G. Wagner, and M. Grundmann, "Ballistic propagation of exciton-polariton condensates in a ZnO-based microcavity," *New J. Phys.* **14**(1), 013037 (2012).
8. T. C. Lu, Y.-Y. Lai, Y.-P. Lan, S.-W. Huang, J.-R. Chen, Y.-C. Wu, W.-F. Hsieh, and H. Deng, "Room temperature polariton lasing vs. photon lasing in a ZnO-based hybrid microcavity," *Opt. Express* **20**(5), 5530–5537 (2012).
9. X. Liu, T. Galfsky, Z. Sun, F. Xia, E.-c. Lin, Y.-H. Lee, S. Kéna-Cohen, and V. M. Menon, "Strong light-matter coupling in two-dimensional atomic crystals," *Nat. Photonics* **9**(1), 30–34 (2015).
10. S. Dufferwiel, S. Schwarz, F. Withers, A. A. P. Trichet, F. Li, M. Sich, O. Del Pozo-Zamudio, C. Clark, A. Nalitov, D. D. Solnyshkov, G. Malpuech, K. S. Novoselov, J. M. Smith, M. S. Skolnick, D. N. Krizhanovskii, and A. I. Tartakovskii, "Exciton-polaritons in van der Waals heterostructures embedded in tunable microcavities," *Nat. Commun.* **6**(1), 8579 (2015).
11. S. Wang, S. Li, T. Chervy, A. Shalabney, S. Azzini, E. Orgiu, J. A. Hutchison, C. Genet, P. Samorì, and T. W. Ebbesen, "Coherent coupling of WS<sub>2</sub> monolayers with metallic photonic nanostructures at room temperature," *Nano Lett.* **16**(7), 4368–4374 (2016).

12. X. Liu, W. Bao, Q. Li, C. Ropp, Y. Wang, and X. Zhang, "Control of coherently coupled exciton polaritons in monolayer tungsten disulphide," *Phys. Rev. Lett.* **119**(2), 027403 (2017).
13. S. Wang, Q. Le-Van, F. Vaianella, B. Maes, S. Eizagirre Barker, R. H. Godiksen, A. G. Curto, and J. Gomez Rivas, "Limits to strong coupling of excitons in multilayer WS<sub>2</sub> with collective plasmonic resonances," *ACS Photonics* **6**(2), 286–293 (2019).
14. S. Dhara, C. Chakraborty, K. M. Goodfellow, L. Qiu, T. A. O'Loughlin, G. W. Wicks, S. Bhattacharjee, and A. N. Vamivakas, "Anomalous dispersion of microcavity trion-polaritons," *Nat. Phys.* **14**(2), 130–133 (2018).
15. L. Liu, L. Y. M. Tobing, X. Yu, J. Tong, B. Qiang, A. I. Fernández-Domínguez, F. J. Garcia-Vidal, D. H. Zhang, Q. J. Wang, and Y. Luo, "Strong plasmon–exciton interactions on nanoantenna array–monolayer WS<sub>2</sub> hybrid system," *Adv. Opt. Mater.* **8**(5), 1901002 (2020).
16. M. Ramezani, Q. Le-Van, A. Halpin, and J. Gómez Rivas, "Nonlinear emission of molecular ensembles strongly coupled to plasmonic lattices with structural imperfections," *Phys. Rev. Lett.* **121**(24), 243904 (2018).
17. T. K. Hakala, A. J. Moilanen, A. I. Väkeväinen, R. Guo, J.-P. Martikainen, K. S. Daskalakis, H. T. Rekola, A. Julku, and P. Törmä, "Bose-einstein condensation in a plasmonic lattice," *Nat. Phys.* **14**(7), 739–744 (2018).
18. I. Suárez, M. Vallés-Pelarda, A. F. Gualdrón-Reyes, I. Mora-Seró, A. Ferrando, H. Michinel, J. R. Salgueiro, and J. P. M. Pastor, "Outstanding nonlinear optical properties of methylammonium- and Cs-Pb<sub>x</sub> (x = br, i, and br–i) perovskites: Polycrystalline thin films and nanoparticles," *APL Mater.* **7**(4), 041106 (2019).
19. D. Liu, J. Liu, K. Zhang, P. Wang, C. Miao, J. Sun, B. Zhang, J. He, X. Hao, and Z.-x. Yang, "Giant nonlinear optical response of lead-free all-inorganic csnbr<sub>3</sub> nanoplates," *J. Phys. Chem. C* **125**(1), 803–811 (2021).
20. P. Chen, Y. Bai, M. Lyu, J.-H. Yun, M. Hao, and L. Wang, "Progress and perspective in low-dimensional metal halide perovskites for optoelectronic applications," *Sol. RRL* **2**(3), 1700186 (2018).
21. C. M. Mauck and W. A. Tisdale, "Excitons in 2d organic–inorganic halide perovskites," *Trends Chem.* **1**(4), 380–393 (2019).
22. M. Baranowski and P. Plochocka, "Excitons in metal-halide perovskites," *Adv. Energy Mater.* **10**(26), 1903659 (2020).
23. T. Fujita, Y. Sato, T. Kuitani, and T. Ishihara, "Tunable polariton absorption of distributed feedback microcavities at room temperature," *Phys. Rev. B* **57**(19), 12428–12434 (1998).
24. P. Bouteyre, H. S. Nguyen, J.-S. Lauret, G. Trippé-Allard, G. Delport, F. Lédée, H. Diab, A. Belarouci, C. Seassal, D. Garrot, F. Bretenaker, and E. Deleporte, "Room-temperature cavity polaritons with 3-d hybrid perovskite: Toward large-surface polaritonic devices," *ACS Photonics* **6**(7), 1804–1811 (2019).
25. L. Polimeno, A. Fieramosca, G. Lerario, M. Cinquino, M. De Giorgi, D. Ballarini, F. Todisco, L. Dominici, V. Ardizzone, M. Pugliese, C. T. Prontera, V. Maiorano, G. Gigli, L. De Marco, and D. Sanvitto, "Observation of two thresholds leading to polariton condensation in 2-d hybrid perovskites," *Adv. Opt. Mater.* **8**(16), 2000176 (2020).
26. W. Niu, L. A. Ibbotson, D. Leipold, E. Runge, G. V. Prakash, and J. J. Baumberg, "Image excitons and plasmon-exciton strong coupling in two-dimensional perovskite semiconductors," *Photonics Res.* **91**(16), 161303 (2015).
27. L. Lu, Q. Le-Van, L. Ferrier, E. Drouard, C. Seassal, and H. S. Nguyen, "Engineering a light-matter strong coupling," *Photon. Res.* **8**(12), A91–A100 (2020).
28. S. Zhang, Q. Shang, W. Du, J. Shi, Z. Wu, Y. Mi, J. Chen, F. Liu, Y. Li, M. Liu, Q. Zhang, and X. Liu, "Strong exciton–photon coupling in hybrid inorganic-organic perovskite micro/nanowires," *Adv. Opt. Mater.* **6**(2), 1701032 (2018).
29. Q. Shang, S. Zhang, Z. Liu, J. Chen, P. Yang, C. Li, W. Li, Y. Zhang, Q. Xiong, X. Liu, and Q. Zhang, "Surface plasmon enhanced strong exciton-photon coupling in hybrid inorganic-organic perovskite nanowires," *Nano Lett.* **18**(6), 3335–3343 (2018).
30. N. H. M. Dang, D. Gerace, E. Drouard, G. Trippé-Allard, F. Lédée, R. Mazurczyk, E. Deleporte, C. Seassal, and H. S. Nguyen, "Tailoring dispersion of room-temperature exciton-polaritons with perovskite-based subwavelength metasurfaces," *Nano Lett.* **20**(3), 2113–2119 (2020).
31. I. A. M. Al-Ani, K. As'Ham, L. Huang, A. E. Miroshnichenko, W. Lei, and H. T. Hattori, "Strong coupling of exciton and high-q mode in all-perovskite metasurfaces," *Adv. Opt. Mater.* **10**(1), 2101120 (2022).
32. Y. Wang, J. Tian, M. Klein, G. Adamo, S. T. Ha, and C. Soci, "Electrically driven exciton-polaritons in metal halide perovskite metatransistors," arXiv arXiv:2209.05810 (2022).
33. G. W. Castellanos, S. Murai, T. Raziman, S. Wang, M. Ramezani, A. G. Curto, and J. Gómez Rivas, "Exciton-polaritons with magnetic and electric character in all-dielectric metasurfaces," *ACS Photonics* **7**(5), 1226–1234 (2020).
34. F. Todisco, R. Malureanu, C. Wolff, P. A. D. Gonçalves, A. S. Roberts, N. A. Mortensen, and C. Tserkezis, "Magnetic and electric mie-exciton polaritons in silicon nanodisks," *Nanophotonics* **9**(4), 803–814 (2020).
35. Z.-T. Huang, C.-W. Yin, Y.-H. Hong, H. Li, K.-B. Hong, T. S. Kao, M.-H. Shih, and T.-C. Lu, "Hybrid plasmonic surface lattice resonance perovskite lasers on silver nanoparticle arrays," *Adv. Opt. Mater.* **9**(17), 2100299 (2021).
36. Q. T. Trinh, S. K. Nguyen, D. H. Nguyen, G. K. Tran, V. H. Le, H.-S. Nguyen, and Q. Le-Van, "Coexistence of surface lattice resonances and bound states in the continuum in a plasmonic lattice," *Opt. Lett.* **47**(6), 1510–1513 (2022).
37. K. Gauthron, J.-S. Lauret, L. Doyennette, G. Lanty, A. A. Choueiry, S. Zhang, A. Brehier, L. Largeau, O. Mauguin, J. Bloch, and E. Deleporte, "Optical spectroscopy of two-dimensional layered (C<sub>6</sub>H<sub>5</sub>C<sub>2</sub>H<sub>4</sub>-NH<sub>3</sub>)<sub>2</sub>-PbI<sub>4</sub> perovskite," *Opt. Express* **18**(6), 5912–5919 (2010).

38. C. Katan, N. Mercier, and J. Even, "Quantum and dielectric confinement effects in lower-dimensional hybrid perovskite semiconductors," *Chem. Rev.* **119**(5), 3140–3192 (2019).
39. S. T. Ha, X. Liu, Q. Zhang, D. Giovanni, T. C. Sum, and Q. Xiong, "Synthesis of organic-inorganic lead halide perovskite nanoplatelets: Towards high-performance perovskite solar cells and optoelectronic devices," *Adv. Opt. Mater.* **2**(9), 838–844 (2014).
40. S. Zhang, P. Audebert, Y. Wei, A. Al Choueiry, G. Lanty, A. Bréhier, L. Galmiche, G. Clavier, C. Boissière, J.-S. Lauret, and E. Deleporte, "Preparations and characterizations of luminescent two dimensional organic-inorganic perovskite semiconductors," *Materials* **3**(5), 3385–3406 (2010).
41. G. Vuye, S. Fisson, V. Nguyen Van, Y. Wang, J. Rivory, and F. Abelès, "Temperature dependence of the dielectric function of silicon using in situ spectroscopic ellipsometry," *Thin Solid Films* **233**(1-2), 166–170 (1993).
42. R. Guo, T. K. Hakala, and P. Törmä, "Geometry dependence of surface lattice resonances in plasmonic nanoparticle arrays," *Phys. Rev. B* **95**(15), 155423 (2017).
43. M. Decker, I. Staude, M. Falkner, J. Dominguez, D. N. Neshev, I. Brener, T. Pertsch, and Y. S. Kivshar, "High-efficiency dielectric Huygens' surfaces," *Adv. Opt. Mater.* **3**(6), 813–820 (2015).
44. L. Carletti, A. Locatelli, O. Stepanenko, G. Leo, and C. D. Angelis, "Enhanced second-harmonic generation from magnetic resonance in algaas nanoantennas," *Opt. Express* **23**(20), 26544–26550 (2015).
45. V. E. Babicheva and A. B. Evlyukhin, "Resonant lattice Kerker effect in metasurfaces with electric and magnetic optical responses," *Laser Photonics Rev.* **11**(6), 1700132 (2017).
46. J. van de Groep and A. Polman, "Designing dielectric resonators on substrates: Combining magnetic and electric resonances," *Opt. Express* **21**(22), 26285–26302 (2013).
47. N. V. Dung, B. S. Tung, B. X. Khuyen, Y. J. Yoo, Y. Lee, J. Y. Rhee, and V. D. Lam, "Metamaterial perfect absorber using the magnetic resonance of dielectric inclusions," *J. Korean Phys. Soc.* **68**(8), 1008–1013 (2016).
48. N. A. Butakov and J. A. Schuller, "Designing multipolar resonances in dielectric metamaterials," *Sci. Rep.* **6**(1), 38487 (2016).
49. S. Murai, G. W. Castellanos, T. V. Raziman, A. G. Curto, and J. G. Rivas, "Enhanced light emission by magnetic and electric resonances in dielectric metasurfaces," *Adv. Opt. Mater.* **8**(16), 1902024 (2020).
50. S. I. Azzam, K. Chaudhuri, A. Lagutchev, Z. Jacob, Y. L. Kim, V. M. Shalaev, A. Boltasseva, and A. V. Kildishev, "Single and multi-mode directional lasing from arrays of dielectric nanoresonators," *Laser Photonics Rev.* **15**(3), 2000411 (2021).
51. Q. M. Ngo, K. Q. Le, D. L. Vu, and V. H. Pham, "Optical bistability based on Fano resonances in single- and double layer nonlinear slab waveguide gratings," *J. Opt. Soc. Am. B* **31**(5), 1054–1061 (2014).
52. F. Monticone and A. Alù, "Metamaterial, plasmonic and nanophotonic devices," *Rep. Prog. Phys.* **80**(3), 036401 (2017).
53. R. Alaee, C. Rockstuhl, and I. Fernandez-Corbaton, "An electromagnetic multipole expansion beyond the long-wavelength approximation," *Opt. Commun.* **407**, 17–21 (2018).
54. D. Gerace and L. C. Andreani, "Quantum theory of exciton-photon coupling in photonic crystal slabs with embedded quantum wells," *Phys. Rev. B* **75**(23), 235325 (2007).
55. S. Zanotti, H. S. Nguyen, M. Minkov, L. C. Andreani, and D. Gerace, "Theory of photonic crystal polaritons in periodically patterned multilayer waveguides," *Phys. Rev. B* **106**(11), 115424 (2022).
56. K. As'ham, I. Al-Ani, W. Lei, H. T. Hattori, L. Huang, and A. Miroshnichenko, "Mie exciton-polariton in a perovskite metasurface," *Phys. Rev. Appl.* **18**(1), 014079 (2022).
57. Y. Yang, G. Yoon, S. Park, S. D. Namgung, T. Badloe, K. T. Nam, and J. Rho, "Revealing structural disorder in hydrogenated amorphous silicon for a low-loss photonic platform at visible frequencies," *Adv. Mater.* **33**(9), 2005893 (2021).